Cellulose
https://doi.org/10.1007/s10570-023-05082-2

ORIGINAL RESEARCH

Electrocatalytic Pt-embedded ZIF-8 on nanocellulose-based flexible conductive electrodes for hydrogen evolution reaction

Nattinee Krathumkhet · Cheng-Yu Kao · Toyoko Imae · Carlos Rodriguez-Abreu

Received: 28 August 2022 / Accepted: 28 January 2023

Abstract Hydrogen fuel cell is a clean green energy device, but it is demanded valid conjugation between catalyst and substrate for generating the effective active site and ion transfer. Here, the hydrogen evolution reaction (HER) efficiency was investigated using Pt-embedded zeolitic imidazolate framework-8 (Pt@ZIF-8) electrocatalysts. Although the Pt content was only 2.8 wt%, the efficiency was equivalent to the reference catalyst (~40 wt% Pt in carbon); The reduction of Pt content improves cost performance and saves resources, making fuel cells more affordable. Furthermore, a flexible substrate consisting of electroconductive sulfonated polypyrrole and TEMPO-oxidized cellulose nanofiber film was found to be effective for embedding Pt@ZIF-8 electrocatalysts, acting as flexible and lightweight electrodes. Moreover, the generated hydrogen easily diffuses through the porous cellulose film. The fabricated electrocatalytic substrates are promising composite materials for hydrogen fuel cells, which consume significantly small amount of noble metal, making the renewable energy production more reasonable.

N. Krathumkhet · T. Imae (✉)
Graduate Institute of Applied Science and Technology, National Taiwan University of Science and Technology, 43 Keelung Road, Section 4, Taipei 10607, Taiwan, ROC
e-mail: imae@mail.ntust.edu.tw

C.-Y. Kao · T. Imae
Department of Chemical Engineering, National Taiwan University of Science and Technology, 43 Keelung Road, Section 4, Taipei 10607, Taiwan, ROC

T. Imae
Department of Materials Science and Engineering, National Taiwan University of Science and Technology, 43 Keelung Road, Section 4, Taipei 10607, Taiwan, ROC

C. Rodriguez-Abreu
Institute of Advanced Chemistry of Catalonia, Spanish National Research Council (IQAC-CSIC), and Networking Research Center on Bioengineering, Biomaterials and Nanomedicine (CIBER-BBN), Jordi Girona 18-26, 08034 Barcelona, Spain

Published online: 15 February 2023

Graphical abstract

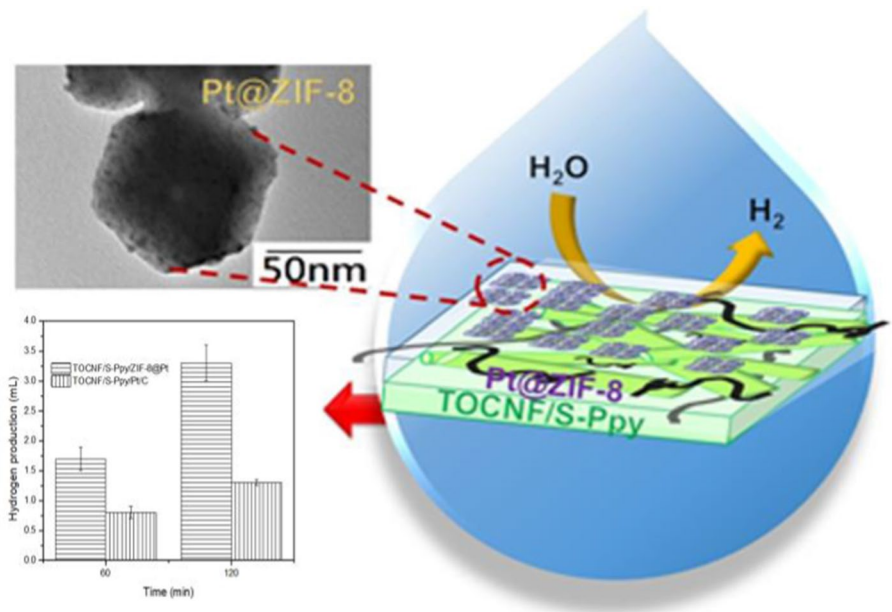

Keywords Hydrogen production · Composite electrode · Caged nanoparticle · Cellulose nanofiber-based flexible substrate · Polypyrrole sulfonation

Introduction

The global climate crisis is mainly derived from human activities, man-made products and burning fossil fuels (Perera 2018). To address these problems, green and renewable energy sources are very important for future development. In this respect, hydrogen is a clean green energy source with many advantages such as availability and high combustion heat value. Renewable sources of hydrogen production are mainly water splitting (electrolysis, thermolysis, and photolysis) and biomass (biological and thermochemical) processes, and one of critical factors is the economical and global scaling up of the hydrogen production (Martino et al. 2021; Agyekumet al. 2022). A hydrogen fuel cell consists of two electrodes namely a positive electrode (cathode) and a negative electrode (anode) separated by a polymer electrolyte membrane (Sarfraz et al. 2020). The cathode electrode also known as the gas diffusion layer (GDL) is a part of the substrate that is coated with electrocatalyst to improve the efficiency of the hydrogen evolution reaction (HER) (Sun et al. 2018). Thus, it regenerates highly purified hydrogen by means of electrochemical water splitting process (Wei et al. 2020). Platinum (Pt) is a noble metal which is commonly used as an active electrocatalyst in hydrogen generation because it processes a very high exchange current density (Devadas et al. 2019). However, the high cost of this catalyst is a drawback in applications at large scale (Jiang et al. 2019).

Thus, it is critical for materials to satisfy the need for cost-effectivity and earth-abundance. For achieving these conditions, there are two ways, one is to find alternative catalysts to platinum (Devadas et al. 2019; Oh et al. 2021), and another is to reduce the amount of platinum. Some researchers have focused on the state-of-the-art investigations regarding catalysts with reduced platinum content as an increase promising strategy of HER performance (Devadas and Imae 2016; Monteiro et al. 2021), including Pt/α-molybdenum carbide (Lin et al. 2017), Pt/FeOx (Qiao et al. 2011), $PtSn_4$ (Boukhvalov et al. 2020), Pt/NiFe@ultrathin graphene layer (Davodi et al. 2021) Pt@ porous carbon matrix, (Zhang et al. 2018a, b), and Pt/nitrogen-doped carbon nanotube (NCNT) (Ma et al. 2017). Moreover, works on encapsulating

Pt in metal–organic frameworks (MOFs) have been published (Wang et al. 2012). MOFs attract much attention as new potential templates or supports for electrocatalysts, because they are porous crystalline materials that consist of a rigid three-dimensional structure with large specific surface areas and controllable pore sizes (Meng et al. 2020). Zeolitic imidazolate frameworks (ZIFs) are one type of MOFs with imidazolate linkers bridging metal centers that permit the adsorption and desorption of organic molecules and the encapsulation of metals (Wang et al. 2013).

For fuel cells, substrates for catalyst should have excellent electrical conductivity, good mechanical properties, suitable reactant permeability, high thermal stability, ease of processing, and low cost. Typical substrates are carbon cloth, carbon paper, and metallic foams (Litster and McLean 2004). However, they have disadvantages such as high cost (Taherian et al. 2018) and inefficient complexation with catalyst, resulting in the reduction of active sites and ion transfer (Liu et al. 2021; Komini Babu et al. 2016). The lamellar accumulation with multiple layer phases enhancing strategies on the electrocatalytic HER performance is one method for improving the limitation of effective loss on the catalytic activity (Lin et al. 2019, 2020).

Cellulose nanofibers (CNF) are alternative materials obtained from bioresources that have been used in numerous fields such as medicine, tissue engineering, and electronics devices because they exhibit excellent physical and biological properties including various mechanical properties, highly thermal and chemical stability, and superior water adsorption (Krathumkhet et al. 2021a, b; Do et al. 2021; Rahmawati et al. 2020). These properties of CNF make this material adequate as potential catalyst substrate with characteristic of fiber network (Shah and Imae 2016; Gupta and Gupta 2015). However, since CNF has no electrical conductivity, conductive materials should be added to improve electron transfer property (Chen et al. 2020). Among conductive materials, semiconducting metals, conducting polymers, and carbon-based materials have been utilized in various applications to enhance electrocatalytic activity, specific surface area, and electron transfer kinetics (Chang and Imae 2018; Krathumkhet et al. 2021a, b).

In this work, the preparation of a Pt electrocatalyst encapsulated in ZIF-8 (Pt@ZIF-8) by three methods is reported, and Pt@ZIF-8 is incorporated into a CNF composite substrate with antimony tin-doped oxide (ATO) or polypyrrole (Ppy) with the lamellar structure by the layer-by-layer deposition. The performance of these materials as catalysts for HER is evaluated. The high HER efficiency and relatively low Pt content of the present system are promising for the improvement of hydrogen fuel cell devices. Thus, the present work proposes the preparation procedure of costless but efficient catalysts which would allow the mass production of hydrogen gas.

Experimental section

Materials

Zinc nitrate hexahydrate ($Zn(NO_3)_2{\cdot}6H_2O$, 98%), potassium tetrachloroplatinate (K_2PtCl_4), anhydrous hexane (C_6H_{14}, 99%), 2-methyl imidazole ($C_4H_6N_2$, 99%), and sulfanilic acid were purchased from Acros Organics, USA. An aqueous sodium hypochlorite (NaOCl) solution (12% available chlorine) was purchased from Shimakyu Pure Chemicals, Japan. Antimony tin doped oxide (ATO) was obtained from Sigma-Aldrich, USA. Sodium borohydride ($NaBH_4$) was bought from Wako Pure Chemical Industries, Japan. Other reagents were commercial grade. Ultrapure water (Yamato, Japan) with a resistivity of 18.2 MΩ cm was used throughout the experiments.

Synthesis of Pt@ZIF-8

A milky white dispersion of ZIF-8 was obtained by mixing 2-methylimidazole (5.67 g) in water (20 ml) and zinc nitrate hexahydrate (0.29 g) in water (2 ml) and stirring for 5 min. The product was washed with water and ethanol by centrifuging at 25,000 rpm and dried 24 h at 40 °C. Synthesis of Pt@ZIF-8 was carried out by three different methods as illustrated in Fig. 1A.

In the direct mixing synthesis method of Pt@ZIF-8 (M1), potassium tetrachloroplatinate (K_2PtCl_4) (0.029 g) in water (1 ml) and sodium borohydride (28 mg) in water (1.25 ml) were mixed, stirred 3 h, and added to a dispersion of ZIF-8 in water (20 ml). After one day, the collected black precipitate was washed three times with water by centrifugation (10,500 rpm) and dried 24 h at 50 °C. The weight

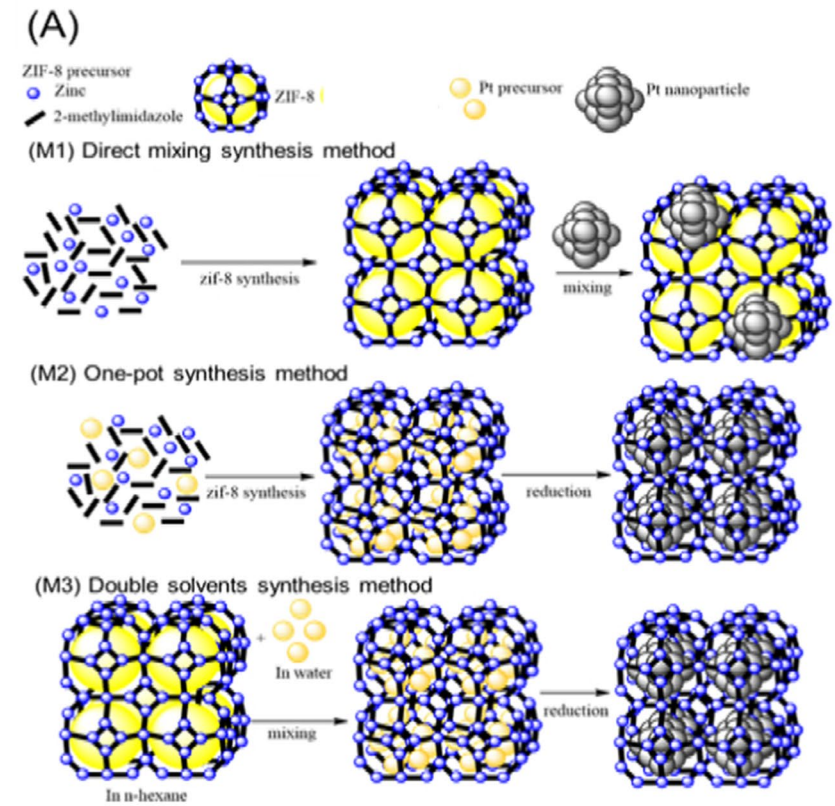

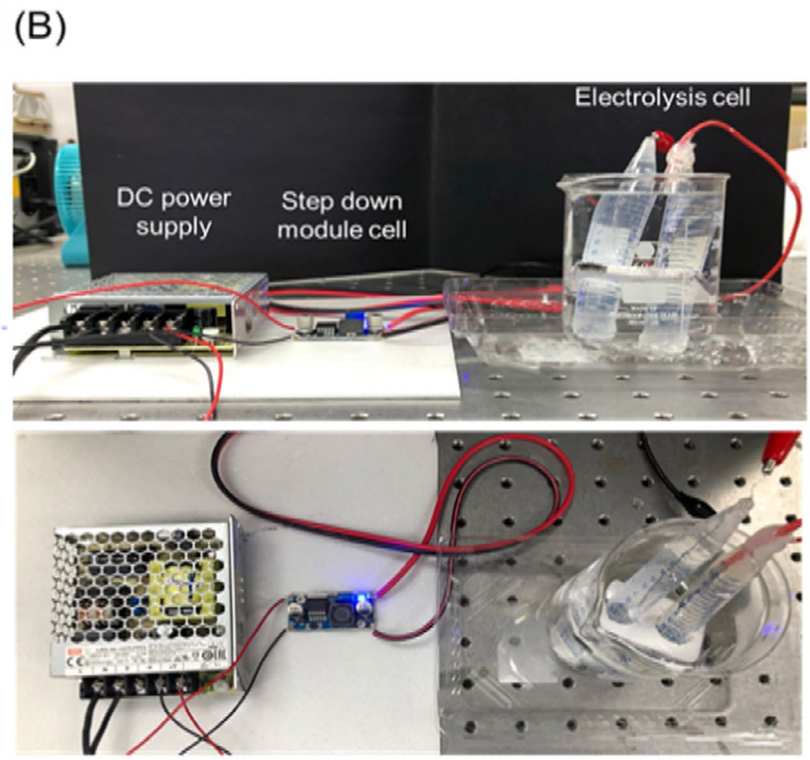

Fig. 1 **A** Synthesis of Pt@ ZIF-8 by three different methods. **B** Electro-station and electrolysis apparatus

ratio of Zinc nitrate hexahydrate: potassium tetrachloroplatinate (Zn: Pt) was 1: 0.1.

In the one-pot synthesis method of Pt@ZIF-8 (M2), 2-methylimidazole (5.67 g) and zinc nitrate hexahydrate (0.29 g) (ZIF-8 precursors) and K_2PtCl_4 (0.029, 0.058, and 0.116 g) at Zn: Pt weight ratio of 1: 0.1, 1: 0.2, and 1: 0.4 were mixed in water and stirred 5 min. The product was washed three times with water by centrifugation (10,500 rpm) and dried 24 h at 50 °C. The yellow precipitate ($PtCl_4^-$@ZIF-8) was dispersed in water (40 ml) and mixed with sodium borohydride (28 mg) in water (1.25 ml). The mixture was stirred 3 h, and the obtained black precipitate was washed and dried 24 h at 40 °C.

In the double solvent synthesis method of Pt@ZIF-8 (M3), ZIF-8 was mixed with n-hexane (30 ml), sonicated 1 h to obtain a homogeneous dispersion, and added K_2PtCl_4 (0.029, 0.058 and 0.116 g) in water (0.3 ml), keeping Zn: Pt weight ratio of 1: 0.1, 1: 0.2, and 1: 0.4. After 24 h, the precipitate was collected by centrifugation at 25,000 rpm and dried 24 h at 40 °C. The yellow precipitate was further dispersed in water (40 ml) and sodium borohydride (28 mg) in water (1.25 ml) was added. The mixture was stirred 3 h, and the obtained black precipitate was washed and dried 24 h at 40 °C.

Preparation of electrode films

Ppy was prepared following a previously reported procedure (Chang and Imae 2018). The sulfonated-Ppy (S-Ppy) was synthesized by dispersing Ppy (50 mg) into a mixed aqueous solution of KNO_3 (2 ml, 6 mM) and HCl (2 ml, 0.1 M) under stirring at 5 °C for 15 min and adding sulfanilic acid (8 ml, 0.06 M) under stirring at 80 °C for 24 h. The product was collected by centrifugation and washed thoroughly with water (Chien et al. 2013).

GDL substrates were prepared from a TEMPO-oxidized cellulose nanofiber (TOCNF, 20 ml, 0.4 wt%) dispersion (Rahmawati et al. 2020) by mixing with ATO or S-Ppy (120 mg) at room temperature (~25 °C) for 2 h. The dispersion was spread into a petri dish (diameter = 7.5 cm) and dried at 40 °C. Pt@ZIF-8 in water (15 mg/ml, 4 ml) was sonicated for 2 min, coated on the dried substrates in the petri dish and then dried at 40 °C for 24 h.

Measurements

The X-ray diffraction (XRD) was recorded at 5–60° and a 4 min^{-1} step on an SC-XR Bruker AXS, D8, USA, with CuKα at 40 kV and 4 mA. N_2 adsorption–desorption isotherms were measured on an Autosorb instrument (Quantachrome, Japan) and analyzed using the Brunauer–Emmett–Teller (BET) equation. All samples were degassed at 30 °C for 12 h before the measurement. The thermal properties were investigated using a thermo gravimetric analyzer (TGA, Q500 TA appliance, USA) for 4–10 mg samples under air flow in a temperature range of 25–800 °C at a 10 °C min^{-1} heating rate. Scanning electron microscopic images were collected on Hitachi TM-1000 at 15 kV and JEOL JSM-6390, Japan, at 50 kV. The samples were attached to stubs by a carbon tape. A transmission electron microscope (TEM, JEOL, Japan) and the high-resolution TEM (HRTEM, Philips Tecnai F30) were operated at 120 and 300 kV, respectively. A drop of sample dispersion (5 µl) was deposited on a copper TEM grid and dried before observation. The infrared absorption spectra were obtained on a FTIR spectrometer (Thermo Nicolet, Nexus 6700, Japan) with 500 scans; samples were embedded in KBr pellets. Electrochemical impedance spectra (EIS) (Zennium—ZAHNER®, Germany) were obtained at 2 MHz–20 Hz. The content of platinum in ZIF-8 was measured by inductively coupled plasma-atomic emission spectroscopy (ICP-AES, Jobin Yvon HORIBA, JY 2000-2, Japan) using standard solutions of platinum precursor at concentrations of 0, 1, 2, 4, 6, 8 and 10 ppm in 2% HNO_3. Then the analyte (Pt@ZIF-8, 100 µg) was treated overnight with an aqua regia (HNO_3:HCl = 1:3 volume ratio) solution (900 µl) to ionize, and the solution was diluted 10 times with a 2% HNO_3 solution to be 10 ppm of Pt@ZIF-8 (10 ml).

Electrochemical measurements

On a glassy carbon electrode (surface area: 0.079 cm^2) polished beforehand with fluff, a dispersion of Pt@ZIF-8 (1 mg/ml, 5 µl) in ethanol was dropped and dried. Then Nafion in ethanol (0.5 wt%, 2 µl) was deposited and subsequently dried. Electrochemical measurements of film electrodes were performed in 0.5 M H_2SO_4 (at acid condition) with an HZ-3000 instrument, Japan, with a linear sweeping

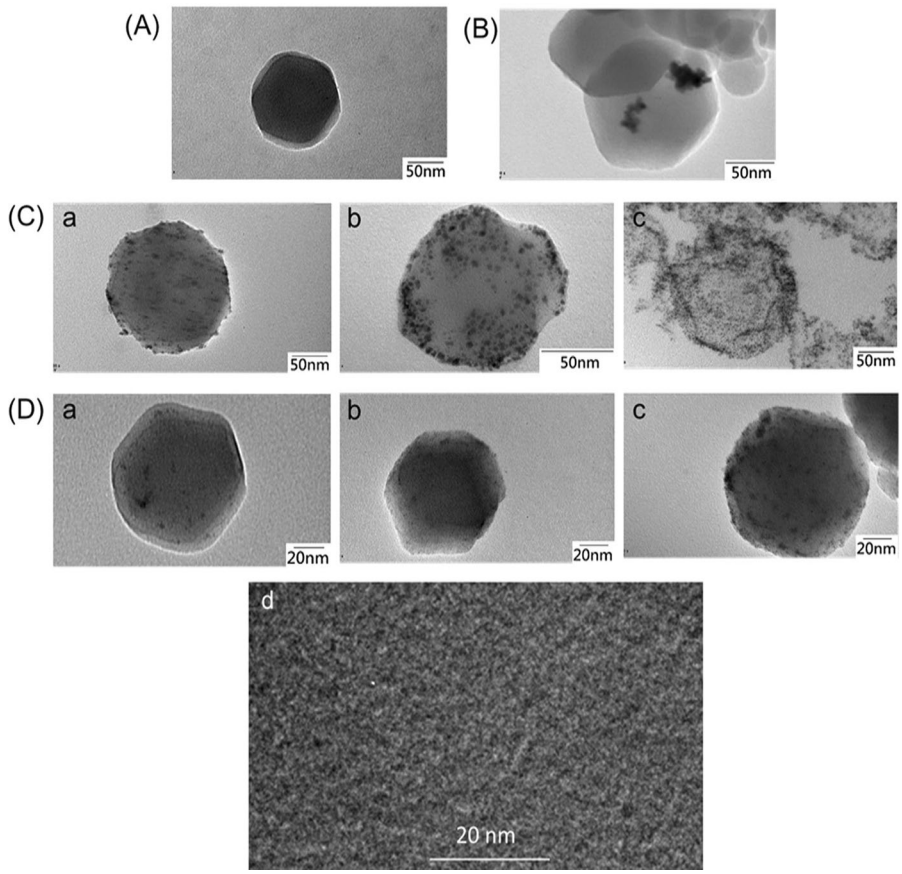

Fig. 2 TEM images of **A** ZIF-8, **B** M1-Pt@ZIF-8 at Zn:Pt weight ratio of 1:0.1, **C** M2-Pt@ZIF-8 at Zn:Pt weight ratio of (a) 1:0.1, (b) 1:0.2 and (c) 1:0.4, and **D** M3-Pt@ZIF-8 at Zn:Pt weight ratio of (a) 1:0.1, (b) 1:0.2 and (c) 1:0.4. (d) and HRTEM image of M3-Pt@ZIF-8 at 1:0.4

voltammetry (LSV) from 0 to −0.8 V and a 5 mV/s scan rate. The H_2 production was measured with electro-station at applied voltage 2.3 V and electrolysis apparatus as shown in Fig. 1B.

Results and discussion

Characterizations of Pt@ZIF-8 materials obtained from three different methods

Pt@ZIF-8 was prepared through three different synthesis routes as illustrated in Fig. 1A**.** In the TEM image of Fig. 2A, ZIF-8 appears as particle with a hexagonal shape and a size of 70–100 nm in agreement with previous reports (Wu et al. 2014; Xu et al. 2018). As seen in the TEM image of M1-Pt@ZIF-8 at Zn:Pt weight ratio of 1:0.1 in Fig. 2B, platinum nanoparticles aggregated on the surface of ZIF-8, suggesting that nanoparticles did not penetrate into ZIF-8 pores because platinum nanoparticles are adsorbed on ZIF-8 easier than encapsulated inside of ZIF-8 due to too large size of platinum nanoparticles for passing through the pore channel in ZIF-8. In contrast, Fig. 2C shows that in M2-Pt@ZIF-8, platinum nanoparticles were embedded into ZIF-8, although a small number of platinum nanoparticles were detected on the surface of ZIF-8 at low platinum ratio (Zn:Pt weight ratio = 1:0.1) (Fig. 2(C)a). However, when the platinum ratio was increased (Zn:Pt weight ratio = 1:0.4), the internal structure of ZIF-8 was inadequately formed, as seen in Fig. 2(C)c, because of too much amount of platinum precursors.

In M3-Pt@ZIF-8, platinum nanoparticles were embedded into ZIF-8 without structural disruption even at Zn:Pt weight ratio of 1:0.4 as shown in Fig. 2(D)a–c. When ZIF-8 uniformly dispersed in nonpolar solvent was mixed with the platinum precursor dispersed in a small amount of polar solvent, the hydrophilic platinum precursor could approach the hydrophilic ZIF-8 pore and be transported into ZIF-8 by the capillary force (Aijaz et al. 2012). Thus, the

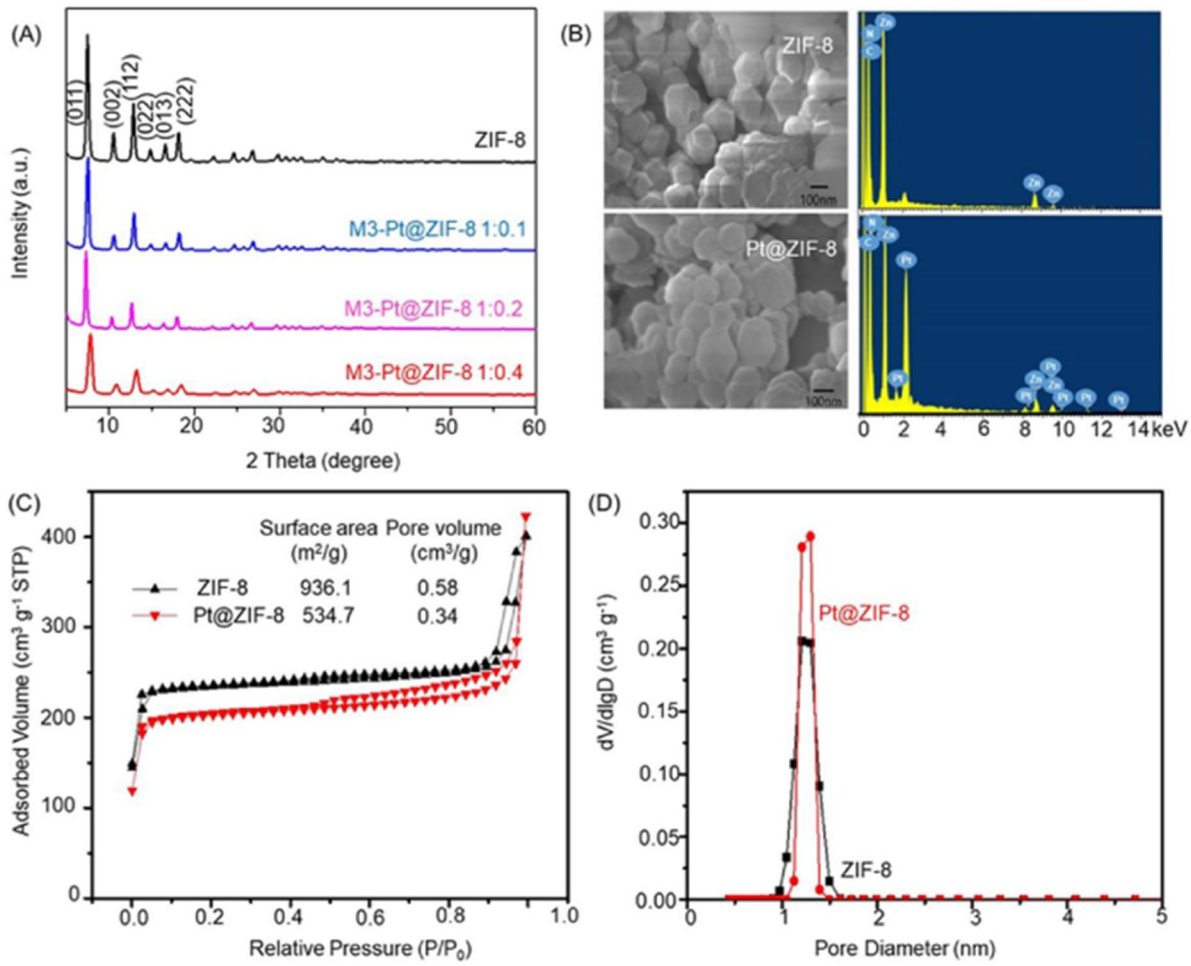

Fig. 3 **A** XRD patterns of ZIF-8 and M3-Pt@ZIF-8 (1:0.1, 1:0.2 and 1:0.4), **B** SEM (left side) and EDX (right side), **C** nitrogen-adsorption/desorption isotherms and **D** pore-size distribution of ZIF-8 and M3-Pt@ZIF-8(1:0.4)

pristine morphology of ZIF-8 was maintained, even when platinum nanoparticles were embedded into the ZIF-8 structure. Figure 2(D)d is an HRTEM image of ZIF-8, where many small black dots with size less than 1 nm to be platinum particles are observed. Thus, M3-Pt@ZIF-8 was selected as the best sample for the following experiments.

The XRD pattern of ZIF-8 (Fig. 3 A) features Bragg peaks at $2\theta = 7.4°$, 10.3°, 12.6°, 14.5°, 16.4°, and 17.9°, corresponding to (011), (002), (112), (022), (013) and (222) planes, respectively, in agreement with the literature (Nordin et al. 2017; Zhang et al. 2018a, b). The XRD of M3-Pt@ZIF-8 showed no significant variations relative to that of the ZIF-8, i.e. the crystalline structure is maintained even after platinum doping. The main Bragg peak ((111) plane) of platinum at $2\theta = 39^{o}$ (Kumar et al. 2017) was not identified in the XRD pattern of M3-Pt@ZIF-8, probably due to the low Pt content.

The SEM image of ZIF-8 powder in Fig. 3B shows nanocrystals of approximately 50–100 nm size with sharp hexagonal facets, similar to that

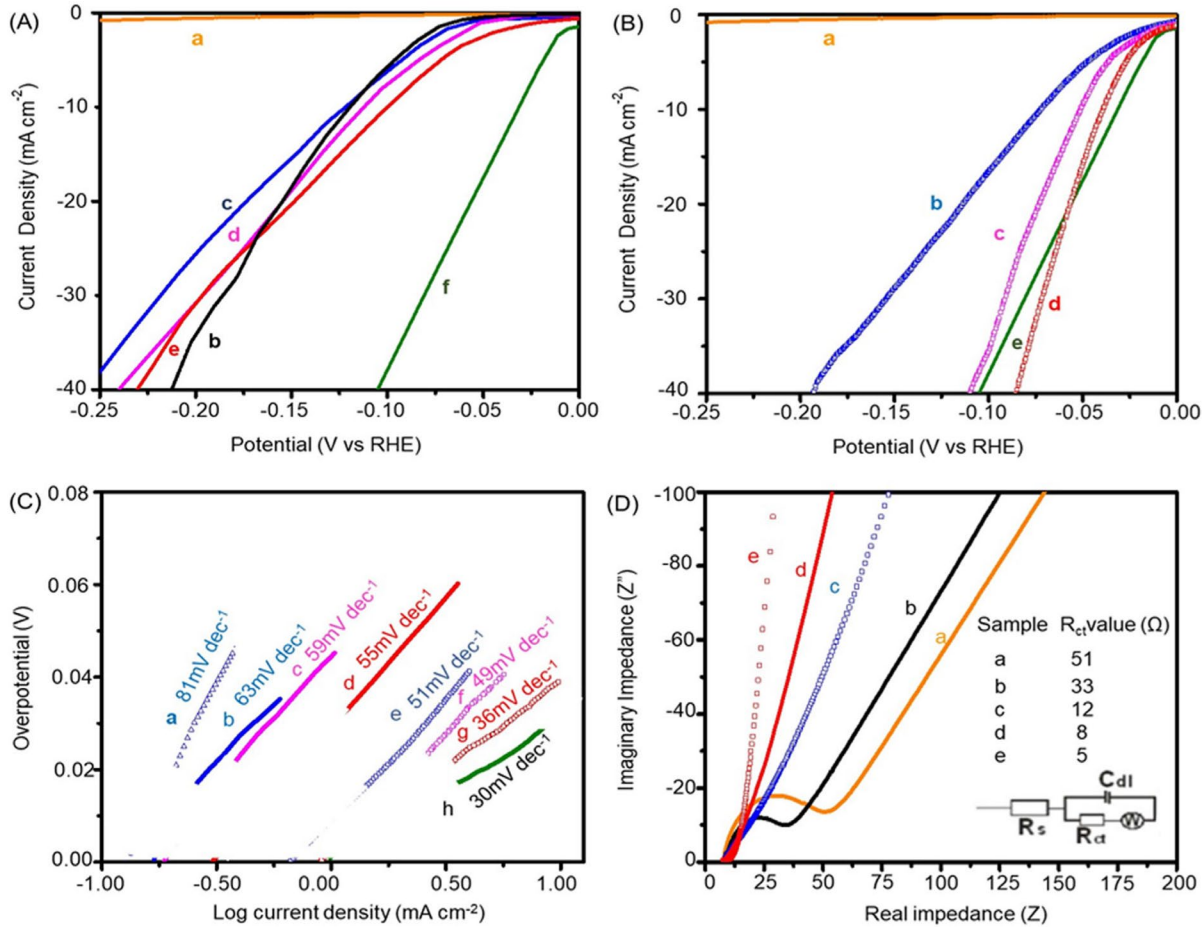

Fig. 4 **A** HER polarization curves of (a) bare electrode, (b) M1-Pt@ZIF-8(1:0.1), (c) M2-Pt@ZIF-8(1:0.1), (d) M2-Pt@ZIF-8(1:0.2), (e) M2-Pt@ZIF-8(1:0.4), and (f) Pt(40 wt%)/C, **B** (a) bare electrode, (b) M3-Pt@ZIF-8(1:0.1), (c) M3-Pt@ZIF-8(1:0.2), (d) M3-Pt@ZIF-8(1:0.4), and (e) Pt(40 wt%)/C. **C** Tafel plots for (a) M1-Pt@ZIF-8(1:0.1), (b) M2-Pt@ZIF-8(1:0.1), (c) M2-Pt@ZIF-8(1:0.2), (d) M2-Pt@ZIF-8(1:0.4), (e) M3-Pt@ZIF-8(1:0.1), (f) M3-Pt@ZIF-8(1:0.2), (g) M3-Pt@ZIF-8(1:0.4), and (h) Pt(40 wt%)/C, and **D** EIS spectra of (a) bare electrode, (b) ZIF-8, (c) M3-Pt@ZIF-8(1:0.1), (d) M3-Pt@ZIF-8(1:0.2), (e) M3-Pt@ZIF-8(1:0.4). Inset is the equivalent Randles circuit used for theoretical analysis

obtained from TEM. The size of M3-Pt@ZIF-8 particles was not significantly different from pristine ZIF-8, The elemental analysis (EDX spectrum) of M3-Pt@ZIF-8 confirmed that Pt is contained in ZIF-8. The Pt content in M3-Pt@ZIF-8 (Zn:Pt = 1:0.4) was 2.82 wt% according to ICP-AES analysis.

N_2 gas adsorption/desorption isotherms at 77 K are shown in Fig. 3C. The specific surface area and pore volume of Pt@ZIF-8 were lower than those of pristine ZIF-8 due to the filling of Pt in ZIF-8 pores. The pore size distribution in Pt@ZIF-8, as seen in Fig. 3D was unimodal with a range 1.0–1.5 nm, similarly to the pore size distribution of ZIF-8 (0.9–1.6 nm). This pore size allows the incorporation of platinum nanoparticles.

HER activity of Pt@ZIF-8 catalyst electrodes

Figure 4A, B shows HER polarization curves of three different Pt@ZIF-8 catalyst electrodes. The initial potential gradually decreased, indicating that the electrocatalytic effect is gradually enhanced. The overpotential at −50 mV increased significantly with increasing Pt content in the order of 0, 2.56 and 16 mA cm^{-2}, respectively, for M1-, M2- and M3-Pt@

Table 1 Comparison of Pt contents and HER results between present and reported electrocatalysts

Electrocatalyst*	Pt content (wt%)	Onset potential (mV)	Current density	Tafel slope (mV/decade)	Reference
Pt(40 wt%)/C	40	0	17 mA/cm^2 at 50 mV	32	This work
M1-Pt@ZIF-8(1:0.1)	–	−73	0.49 mA/cm^2 at 50 mV	81	This work
M2-Pt@ZIF-8(1:0.4)	–	−31	2.56 mA/cm^2 at 50 mV	55	This work
M3-Pt@ZIF-8(1:0.4)	2.82	−5	16 mA/cm^2 at 50 mV	36	This work
GO/DenPtNPs	1.12	−26	0.4 mA/cm^2 at 50 mV	58	Devadas and Imae (2016)
CNH/DenPtNPs	0.86	−16	2.5 mA/cm^2 at 50 mV	53	Devadas and Imae (2016)
CNT/DenPtNPs	1.03	−16	2.5 mA/cm^2 at 50 mV	42	Devadas and Imae (2016)
Pt@PCM	0.095	−281	6 mA/cm^2 at 200 mV	132	Zhang et al. (2018a, b)
Pt/NCNT	0.74	–	10 mA cm^{-2} at 40 mV	33	Ma et al. (2017)
Pt/MoS_2/carbon fiber	2.03	–	0.09 mA/cm^2 at 200 mV	53.6	Hou et al. (2015)
PtP_2@PNC	3.50	–	10 mA/cm^2 at 183 mV	30	Pu et al. (2020)
Pt@MOF-808-EDTA	9.58	−42.1	10 mA/cm^2 at 50 mV	24.4	Li et al. (2019)
PtCu-MoO_2@C	11.3	−42	10 mA/cm^2 at 24 mV	36	Zhang et al. (2020)

*PCM, porous carbon matrix; EDTA, ethylenediaminetetraacetic acid; NCNT, nitrogen-doped carbon nanotube; CNT, carbon nanotube; CNH, carbon nanohorn; GO, graphene oxide; DenPtNP, platinum nanoparticle-encapsulated dendrimer; MoS_2, molybdenum disulphide; CF, carbon fiber; PtP_2, platinum phosphide; PNC, phosphorus and nitrogen dual-doped carbon; MoO_2@C, porous octahedral carbon matrix

ZIF-8, where the value of M3-Pt@ZIF-8 was quite close to 17 mA cm^{-2} of the standard electrode (Pt(40 wt%)/C). The LSV polarization curves were converted to Tafel slope to evaluate the catalytic performance of electrode based on three mechanisms of hydrogen evolution reaction of (I) Volmer reaction (120 mV/dec), (II) Heyrovsky reaction (40 mV/dec) and (III) Tafel reaction (30 mV/dec) (Devadas and Imae 2016). The Tafel slope value of 36 mV/dec for M3-Pt@ZIF-8 indicates that the reaction would theoretically take place via the Volmer-Heyrovsky mechanism and the Volmer-Tafel mechanism, while the Tafel slope of 30 mV/dec for Pt(40 wt%)/C confirms the Volmer-Tafel mechanism (Kumar et al. 2017, 2020; Li et al. 2011) (see Fig. 4C). Then the hydrogen production by a Volmer-Tafel mechanism is preferable over a Volmer-Heyrovsky mechanism, because less mount of electron concerns in the rection.

The impedance characteristics of M3-Pt@ZIF-8 catalyst electrodes are compared to bare and ZIF-8 electrodes in Fig. 4D. The bare and ZIF-8 electrodes showed highelectron transfer resistance (R_{ct}) values (51 and 33 Ω, respectively), indicating the low electron transfer rate. With increasing Pt content against ZIF-8, R_{ct} value decreased to 12, 8, and 5 Ω. That is, the electrode with M3-Pt@ZIF-8(1:0.4) provided the lowest R_{ct} value, demonstrating that M3-Pt@ZIF-8(1:0.4) provides the fastest electron transfer on the HER reaction.

Table 1 shows the comparison of Pt-based electrocatalysts for HER. Particles in the list have far smaller platinum contents than the standard sample (Pt(40 wt%)/C). The Pt content is smaller than 3 wt% (Devadas and Imae 2016; Hou et al. 2015) except for PtP_2@PNC (3.5 wt%), Pt@MOF-808-EDTA (9.58 wt%) and PtCu-MoO_2@C (11.3 wt%) with current density of 10 mA/cm (Pu et al. 2020; Zhang et al. 2020; Martino et al. 2021). However, the onset potential of M3-Pt@ZIF-8 was close to that of Pt(40 wt%)/C and lower than those of other Pt-based electrodes (Devadas and Imae 2016; Li et al. 2019). Tafel slope (36 mV/decade) of M3-Pt@ZIF-8 electrocatalysts was also similar to that of Pt(40 wt%)/C and Pt@MOF-808-EDTA but lower than other electrodes. Although Pt/NCNT has a smaller Pt content (0.17 wt%) and Tafel slope (33 mV/decade), as well as PtCu-MoO_2@C with Tafel slope of 30 mV/decade, than M3-Pt@ZIF-8, it had a lower current density (10 mA/cm^2) than M3-Pt@ZIF-8 and Pt(40 wt%)/C. Thus, M3-Pt@ZIF-8 is excellent from the viewpoint of the electrocatalytic activity towards HER alongside of the standard Pt(40 wt%)/C, but it is far better than Pt(40 wt%)/C in terms of the cost performance.

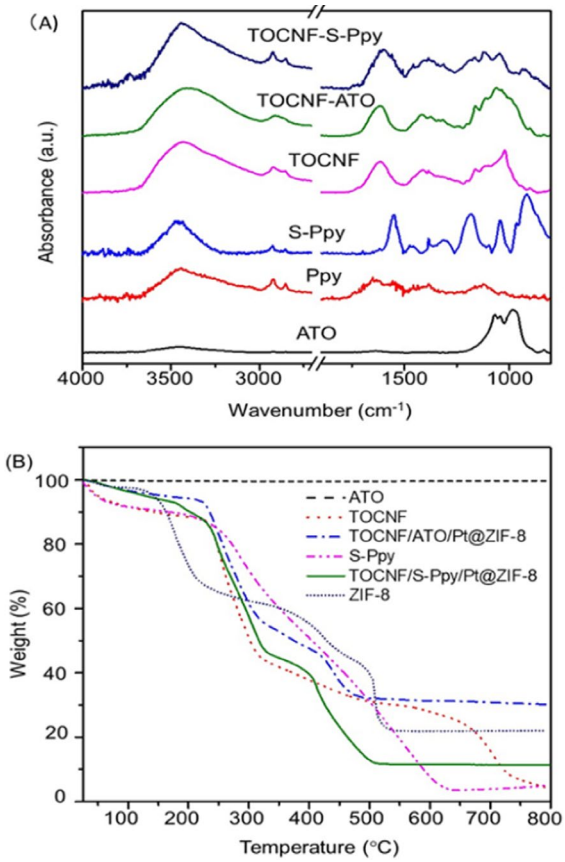

Fig. 5 **A** FTIR absorption spectra of ATO, Ppy, S-Ppy, TOCNF, TOCNF/ATO, and TOCNF/S-Ppy and **B** TGA of ATO, TOCNF, TOCNF/ATO/Pt@ZIF-8, S-Ppy, TOCNF/S-Ppy/Pt@ZIF-8, and ZIF-8

Characterizations of TOCNF/ATO and TOCNF/S-Ppy substrates

The FTIR spectrum of TOCNF (Fig. 5A) shows a characteristic broad band of an O–H stretching vibration mode at 3600–3100 cm^{-1}. Bands at 1610 and 1420 cm^{-1} are assigned to antisymmetric and symmetric stretching vibration modes of COO^- groups, respectively, although they are overlapped on O–H and C–H bending modes, respectively. A band at 1154 cm^{-1} points to C–O–H out-of-plane bending, while a C–O–C stretching mode is associated to a strong band at 1029 cm^{-1} (Kebede et al. 2017). An FTIR spectrum of TOCNF/ATO shows additional characteristic bands at 1068 and 980 cm^{-1} due to the O–Sb–O and O–Sn–O vibration modes, respectively. An IR band of TOCNF/S-Ppy observed at 3440 cm^{-1} is assigned to an N–H stretching vibration mode of Ppy, whereas stretching bands of O–S–O and S=O groups are at 1047 and 948 cm^{-1}, respectively.

Figure 5B shows the thermal decomposition profiles of materials. TOCNF was decomposed through three weight loss steps except the removal of water and residual solvent below 150 °C. A first weight loss between 230 and 350 °C was attributed to cellulose depolymerization. The second thermal degradation was assigned to polymer backbone degradation, which occurred at ~ 500 °C (Shah and Imae 2017). The third degradation step at 650–720 °C indicates decomposition of the oxidized fiber attributed to carbonization through a self-sustained exothermic process (Kebede et al. 2017). ZIF-8 exhibited the first weight loss in temperature range of 25–200 °C, corresponding to the removal of solvent molecules from the cavities (Lo et al. 2016; Pan et al. 2011). Then, a second thermal degradation up to 500 °C corresponds to the degradation of organic ligands namely 2-methylimidazole of ZIF-8 (Li et al. 2020). In addition, ATO slowed no weight loss, but S-Ppy was almost decomposed up to 630 °C (residue = ~ 4.8 wt%). The thermal degradation of TOCNF/ATO/Pt@ZIF-8 and TOCNF/S-Ppy/Pt@ZIF-8 follows the degradation of their components (TOCNF, or S-Ppy and ZIF-8), although the third degradation of TOCNF at 650–720 °C was not observed. The high residue (30.2 wt%) of TOCNF/ATO/Pt@ZIF-8 above 500 °C is attributed to ATO, inorganic moiety of ZIF-8, and Pt. The residue (11.4 wt%) of TOCNF/S-Ppy/Pt@ZIF-8 probably consists of inorganic moieties of ZIF-8 and Pt.

The cross-sectional and surface morphologies of electrode films were observed by SEM. The electrode films prepared by coating Pt@ZIF-8 on TOCNF/ATO or TOCNF/S-Ppy film have a layered morphology as shown in Fig. 6A(a, b), where an upper layer is Pt@ZIF-8 and a bottom layer is TOCNF/ATO or TOCNF/S-Ppy. It was elucidated from Fig. 6A(c–g) that Pt@ZIF-8 consists of aggregates of ZIF-8 nanoparticles, ATO isd large particles with flat faces, S-Ppy is a network of flexible chains. SEM images of TOCNF/ATO and TOCNF/S-Ppy were characterized by large particles of ATO and chain-like texture of S-Ppy, respectively, reflecting the presence of component materials. Especially, S-Ppy shows a chain-like texture combined with fibrous TOCNF that provided the flexibility of an electrode film more than TOCNF/ATO

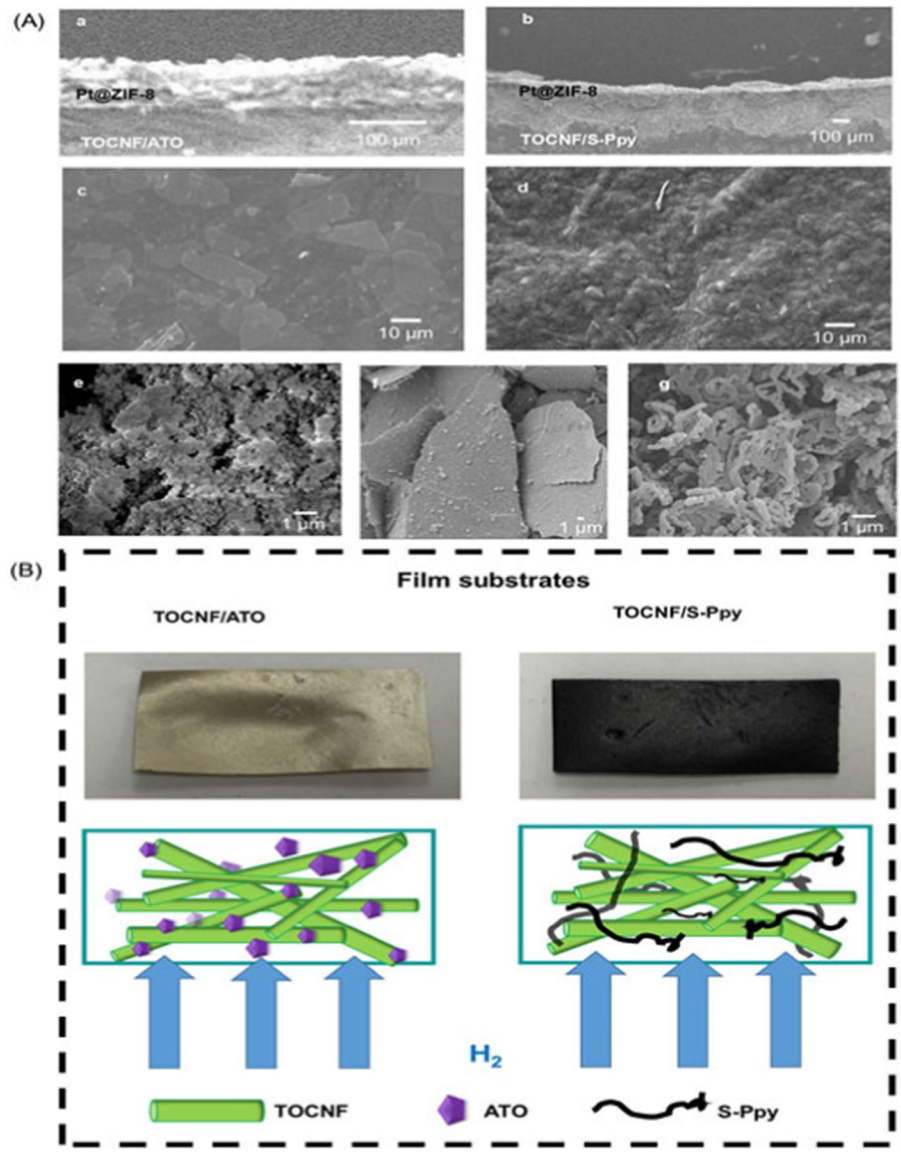

Fig. 6 **A** Cross-sectional SEM images of film substrates of (a) TOCNF/ATO/Pt@ZIF-8 and (b) TOCNF/S-Ppy/Pt@ZIF-8, and surface SEM images of (c) TOCNF/ATO, (d) TOCNF/S-Ppy (e) Pt@ZIF-8, (f) ATO, and (g) S-Ppy. **B** Photos and structural schemes of TOCNF/ATO and TOCNF/S-Ppy film substrate for H_2 gas diffusion

and, moreover, net-like texture of TOCNF/S-Ppy may promote the permeation of H_2 more than TOCNF/ATO as shown in Fig. 6B.

HER activity of electrode films

EIS of electrode films was analyzed to examine the electron transfer resistance (see Fig. 7A). The electron transfer resistance (R_{ct}) of electrodes was calculated based on a Randles circuit model. The TOCNF/ATO and TOCNF/S-Ppy substrates without catalyst-loading exhibited large R_{ct} values of 2.4 and 1.8 Ω, respectively, indicating the rather poor charge transport. After Pt@ZIF-8 catalyst was loaded, both TOCNF/ATO and TOCNF/S-Ppy substrates showed smaller R_{ct} values (1.5 Ω and 0.9 Ω, respectively), verifying the increase of charge transport. The relaxation time constant (τ parameter) on the relaxation process of the electrical double layer was determined from a phase angle maximum of the Bode plot (Fig. 7B) using an equation $\tau = 1/2\pi f$, where f is the relaxation frequency (Kumar et al. 2020). The relaxation time constants for TOCNF/S-Ppy/Pt@ZIF-8, TOCNF/ATO/Pt@ZIF-8, TOCNF/S-Ppy, and TOCNF/ATO were 1.8, 1.5, 1.0, and 0.6 ms, respectively. The higher relaxation time of TOCNF/S-Ppy/

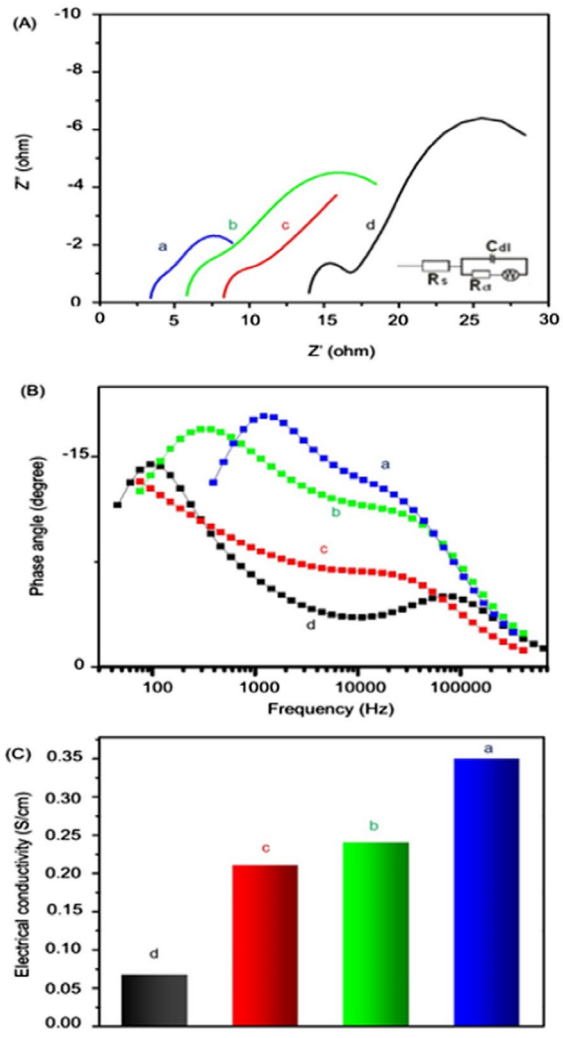

Fig. 7 **A** EIS spectra (inset: a Randles circuit model), **B** Bode plot and **C** electrical conductivity of (a) TOCNF/S-Ppy/Pt@ZIF-8, (b) TOCNF/ATO/Pt@ZIF-8, (c) TOCNF/S-Ppy, and (d) TOCNF/ATO

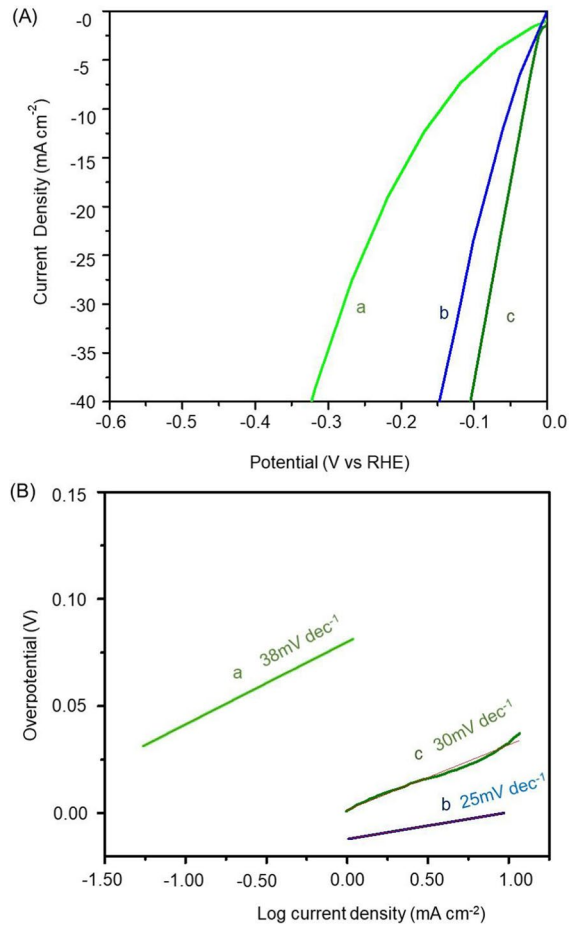

Fig. 8 **A** HER polarization curves and **B** Tafel plots of (a) TOCNF/ATO/Pt@ZIF-8, (b) TOCNF/S-Ppy/Pt@ZIF-8 and (c) Pt(40 wt%)/C

Pt@ZIF-8 suggests its more efficient electrochemical reaction. EIS results were also used to calculate electrical conductivity σ (S/cm) by $\sigma = l/R \times A$ (Tangkitthanachoke et al. 2017), where R is the resistance (Ω), l is the thickness (cm), and A is the area (cm^2). Here, $l = \sim 0.16$ cm and A = 1 cm^2. As shown in Fig. 7C, the electrical conductivity increased in the order of TOCNF/ATO < TOCNF/S-Ppy < TOCNF/ATO/Pt@ZIF-8 < TOCNF/S-Ppy/Pt@ZIF-8. Thus, TOCNF/S-Ppy/Pt@ZIF-8 performs efficiently the electrochemical reaction due to the high electrical conductivity.

Figure 8A, B shows HER polarization and Tafel slope curves for two electrodes. The overpotentials of electrodes at a current density of 40 mA/cm^2 were − 321 and − 147 mV and Tafel slope values were 38 and 25 mVdec^{-1} for active Pt@ZIF-8 on TOCNF/ATO and TOCNF/S-Ppy, respectively. The overpotential value of TOCNF/S-Ppy/Pt@ZIF-8 was only slightly higher than those of Pt(40 wt%)/C and Pt@ZIF-8 (Fig. 4B). Thus, TOCNF/S-Ppy is a more promising electrode in HER activity than TOCNF/ATO. The great HER activity of TOCNF/S-Ppy/Pt@ZIF-8 rises from its high electrical conductivity (Fig. 7C) which may be promoted by the network structure of flexible S-Ppy chains, free voids in

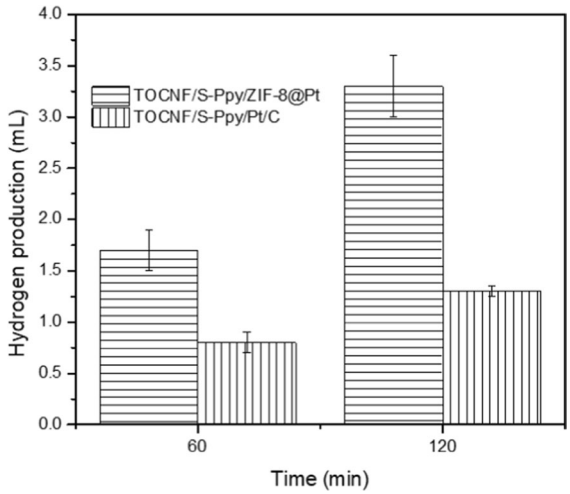

Fig. 9 Hydrogen production from TOCNF/S-Ppy/Pt@ZIF-8 and TOCNF/S-Ppy/Pt(40 wt%)/C electrodes (0.5×3 cm electrode films) at 1.5 V in 0.5 M H_2SO_4

network and a rough aggregate structure of Pt@ZIF-8 (Fig. 6A). Then electrons pass effectively through the TOCNF/S-Ppy/Pt@ZIF-8 electrode, but the electron-passing is not easy in an ATO-including electrode because of the compact morphology of ATO. The open structure of TOCNF/S-Ppy/Pt@ZIF-8 electrode may be available as gas channel (Fig. 6B). Moreover, the TOCNF/S-Ppy/Pt@ZIF-8 film electrode was more effective than Pt@ZIF-8 on a glassy carbon electrode. Thus, the former electrode is superior for practical application.

As shown in Fig. 9., the H_2 production rates of TOCNF/S-Ppy/Pt@ZIF-8 (2.8 wt% Pt content) and TOCNF/S-Ppy/Pt(40 wt%)/C were 1.7 mL/min H_2 and 0.8 mL/min H_2, respectively, at 60 min; the H_2 production increased after 120 min. The results proved that Pt@ZIF-8 can produce more H_2 than Pt(40 wt%)/C. Moreover, the hydrogen generation on TOCNF/S-Ppy/Py@ZIF-8 was almost double (98%) at 120 min in comparison with it at 60 min, but it on TOCNF/S-Ppy/Pt(40 wt%)/C at 120 min was only 81% of double of amount at 60 min. This indicates that Pt in ZIF-8 is stable different from Pt(40 wt%)/C, which was simply adsorbed on TOCNF/S-Ppy. Thus, Pt@ZIF-8 is a good candidate as cost-effective, low Pt content and stable electrocatalyst for HER.

Conclusions

This work demonstrated the efficiency of an electrocatalyst on HER using Pt@ZIF-8, which has a platinum content of only 2.8 wt% and a Tafel slope of 36 mV/decade, keeping the distributed metal active sites in ZIF-8. The efficiency was comparable to a standard Pt(40 wt%)/C electrode, indicating that Pt@ZIF-8 has a merit of low amount of platinum. The electrocatalyst was deposited on flexible conducting substrate electrode via the layer-on-layer method. The potential of the substrate occurred by structural contribution of TOCNF/S-Ppy with better conductivity and void volume for electron transfer and gas diffusion in a comparison with TOCNF/ATO. Moreover, a TOCNF/S-Ppy/Pt@ZIF-8 electrode generated larger volume of H_2 gas than a Pt(40 wt%)/C electrode. As a result, it can be concluded that the material preparation based on catalyst-embedded MOF-coated conducting flexible film electrode promotes effective hydrogen generation. Thus, this report promises a future benefit in fuel cells development with improved cost performance.

Acknowledgments N.K. was financially supported by National Taiwan University of Science and Technology, Taiwan, for a student scholarship. The authors would like to acknowledge Adrià Perez-Calm and Jonathan Miras, IQAC-CSIC, for their valuable suggestions and their help in the experiments. The authors want to thank NANBIOSIS ICTS and the Nanostructured Liquid Characterization Unit (U12) for SEM observations.

Authors' contribution NK managed conceptualization, NK, CK worked methodology, investigation, visualization, NK performed writing—original draft the manuscript, TI and CR-A played Supervision, and writing—review and editing the manuscript. CR-A managed funding acquisition.

Funding C.R.-A. is grateful to the financial support from the Spanish Ministry of Economy and Competitiveness (CTQ2017-84998-P project), the European Regional Development Fund, Generalitat de Catalunya (2017SGR01778) and the Networking Research Center on Bioengineering, Biomaterials and Nanomedicine (CIBER-BBN). Support from the I-LINK 1188 project (CSIC) is also acknowledged.

Availability of data and materials Data and materials in the present work are not available.

Declarations

Conflict of interest The authors report no declarations of interest.

Ethical approval Authors follow scientific ethics of the journal.

Consent of publication All authors concentrate for publication.

References

Agyekum EB, Nutakor C, Agwa AM, Kamel S (2022) A critical review of renewable hydrogen production methods: factors affecting their scale-up and its role in future energy generation. Membranes 12(2):173. https://doi.org/10.3390/membranes12020173

Aijaz A, Karkamkar A, Choi YJ, Tsumori N, Rönnebro E, Autrey T, Shioyama H, Xu Q (2012) Immobilizing highly catalytically active Pt nanoparticles inside the pores of metal–organic framework: a double solvents approach. J Am Chem Soc 134(34):13926–13929. https://doi.org/10.1021/ja3043905

Boukhvalov DW, Marchionni A, Filippi J, Kuo CN, Fujii J, Edla R, Edla R, Politano A (2020) Efficient hydrogen evolution reaction with platinum stannide $PtSn_4$ via surface oxidation. J Mater Chem A 8(5):2349–2355. https://doi.org/10.1039/C9TA10097K

Chang CC, Imae T (2018) Synergistic performance of composite supercapacitors between carbon nanohorn and conducting polymer. ACS Sustain Chem Eng 6(4):5162–5172. https://doi.org/10.1021/acssuschemeng.7b04813

Chen Y, Pang L, Li Y, Luo H, Duan G, Mei C, Xu W, Zhou W, Liu K, Jiang S (2020) Ultra-thin and highly flexible cellulose nanofiber/silver nanowire conductive paper for effective electromagnetic interference shielding. Compos Part A Appl Sci Manuf 135:105960. https://doi.org/10.1016/j.compositesa.2020.105960

Chien HC, Tsai LD, Huang CP, Kang CY, Lin JN, Chang FC (2013) Sulfonated graphene oxide/Nafion composite membranes for high-performance direct methanol fuel cells. Int J Hydrog Energy 38(31):13792–13801. https://doi.org/10.1016/j.ijhydene.2013.08.036

Davodi F, Cilpa-Karhu G, Sainio J, Tavakkoli M, Jiang H, Mühlhausen E, Marzun G, Gökce B, Laasonen K, Kallio T (2021) Designing of low Pt electrocatalyst through immobilization on metal@ C support for efficient hydrogen evolution reaction in acidic media. J Electroanal Chem 896:115076. https://doi.org/10.1016/j.jelechem.2021.115076

Devadas B, Imae T (2016) Hydrogen evolution reaction efficiency by low loading of platinum nanoparticles protected by dendrimers on carbon materials. Electrochem Commun 72:135–139. https://doi.org/10.1016/j.elecom.2016.09.022

Devadas B, Chang CC, Imae T (2019) Hydrogen evolution reaction efficiency of carbon nanohorn incorporating molybdenum sulfide and polydopamine/palladium nanoparticles. J Taiwan Inst Chem Eng 102:378–386. https://doi.org/10.1016/j.jtice.2019.05.014

Do TTA, Grijalvo S, Imae T, Garcia-Celma MJ, Rodríguez-Abreu C (2021) A nanocellulose-based platform towards targeted chemo-photodynamic/photothermal cancer therapy. Carbohydr Polym 270:118366. https://doi.org/10.1016/j.carbpol.2021.118366

Gupta KM, Gupta N (2015) Advanced electrical and electronics materials: processes and applications. John Wiley & Sons. https://doi.org/10.1002/9781118998564

Hou D, Zhou W, Liu X, Zhou K, Xie J, Li G, Chen S (2015) Pt nanoparticles/MoS_2 nanosheets/carbon fibers as efficient catalyst for the hydrogen evolution reaction. Electrochim Acta 166:26–31. https://doi.org/10.1016/j.electacta.2015.03.067

Jiang Z, Ren J, Li Y, Zhang X, Zhang P, Huang J, Du C, Chen J (2019) Low-cost high-performance hydrogen evolution electrocatalysts based on Pt-CoP polyhedra with low Pt loading in both alkaline and neutral media. Dalton Trans 48(24):8920–8930. https://doi.org/10.1039/c9dt01118h

Kebede MA, Imae T, Wu CM, Cheng KB (2017) Cellulose fibers functionalized by metal nanoparticles stabilized in dendrimer for formaldehyde decomposition and antimicrobial activity. Chem Eng J 311:340–347. https://doi.org/10.1016/j.cej.2016.11.107

Komini Babu S, Chung HT, Zelenay P, Litster S (2016) Resolving electrode morphology's impact on platinum group metal-free cathode performance using nano-CT of 3D hierarchical pore and ionomer distribution. ACS Appl Mater Interfaces 8(48):32764–32777. https://doi.org/10.1021/acsami.6b08844

Krathumkhet N, Ujihara M, Imae T (2021) Self-standing films of octadecylaminated-TEMPO-oxidized cellulose nanofibrils with antifingerprint properties. Carbohydr Polym 256:117536. https://doi.org/10.1016/j.carbpol.2020.117536

Krathumkhet N, Imae T, Paradee N (2021b) Electrically controlled transdermal ibuprofen delivery consisting of pectin-bacterial cellulose/polypyrrole hydrogel composites. Cellulose 28(18):11451–11463. https://doi.org/10.1007/s10570-021-04259-x(0123456789)

Kumar MN, Govindh BO, Annapurna NO (2017) Green synthesis and characterization of platinum nanoparticles using sapindus mukorossi Gaertn. Fruit pericarp. Asian J Chem 29(11):2541–2544. https://doi.org/10.14233/ajchem.2017.20842A

Kumar S, Sahoo PK, Satpati AK (2020) Insight into the catalytic performance of HER catalysis of noble metal/3D-G nanocomposites. Electrochim Acta 333:135467. https://doi.org/10.1016/j.electacta.2019.135467

Li Y, Zhang WB, Hsieh IF, Zhang G, Cao Y, Li X, Wesdemiotis C, Lotz B, Xiong H, Cheng SZ (2011) Breaking symmetry toward nonspherical Janus particles based on polyhedral oligomeric silsesquioxanes: molecular design, "click" synthesis, and hierarchical structure. J Am Chem Soc 133(28):10712–10715. https://doi.org/10.1021/ja202906m

Li J, Huang H, Li Y, Tang Y, Mei D, Zhong C (2019) Stable and size-controllable ultrafine Pt nanoparticles derived from a MOF-based single metal ion trap for efficient electrocatalytic hydrogen evolution. J Mater Chem A 7(35):20239–20246. https://doi.org/10.1039/c9ta06184c

Li J, Chang H, Li Y, Li Q, Shen K, Yi H, Zhang J (2020) Synthesis and adsorption performance of La@ ZIF-8 composite metal–organic frameworks. RSC Adv 10(6):3380–3390. https://doi.org/10.1039/c9ra10548d

Lin L, Zhou W, Gao R, Yao S, Zhang X, Xu W, Zheng S, Jiang Z, Yu Q, Li YW, Ma D (2017) Low-temperature hydrogen production from water and methanol using Pt/α-MoC catalysts. Nature 544(7648):80–83. https://doi.org/10.1038/nature21672

Lin Z, Wang C, Wang Z, Liu Q, Le C, Lin B, Chen S (2019) The role of conductivity and phase structure in enhancing catalytic activity of CoSe for hydrogen evolution reaction. Electrochim Acta 294:142–147. https://doi.org/10.1016/j.electacta.2018.10.082

Lin Z, Wang Z, Shen S, Chen Y, Du Z, Tao W, Feng S (2020) One-step method to achieve multiple decorations on lamellar MoS_2 to synergistically enhance the electrocatalytic HER performance. J Alloy Comp 834:155217. https://doi.org/10.1016/j.jallcom.2020.155217

Litster S, McLean G (2004) PEM fuel cell electrodes. J Power Sources 130(1–2):61–76. https://doi.org/10.1016/j.jpowsour.2003.12.055

Liu S, Wippermann K, Lehnert W (2021) Mechanism of action of polytetrafluoroethylene binder on the performance and durability of high-temperature polymer electrolyte fuel cells. Int J Hydrog Energy 46(27):14687–14698. https://doi.org/10.1016/j.ijhydene.2021.01.192

Lo Y, Lam CH, Chang CW, Yang AC, Kang DY (2016) Polymorphism/pseudopolymorphism of metal–organic frameworks composed of zinc (II) and 2-methylimidazole: synthesis, stability, and application in gas storage. RSC Adv 6(92):89148–89156. https://doi.org/10.1039/c6ra19437k

Ma R, Zhou Y, Wang F, Yan K, Liu Q, Wang J (2017) Efficient electrocatalysis of hydrogen evolution by ultralow-Pt-loading bamboo-like nitrogen-doped carbon nanotubes. Mater Today Energy 6:173–180. https://doi.org/10.1016/j.mtener.2017.10.003

Martino M, Ruocco C, Meloni E, Pullumbi P, Palma V (2021) Main hydrogen production processes: an overview. Catalysts 11(5):547. https://doi.org/10.3390/catal11050547

Meng J, Liu X, Niu C, Pang Q, Li J, Liu F, Liu Z, Mai L (2020) Advances in metal–organic framework coatings: versatile synthesis and broad applications. Chem Soc Rev 49(10):3142–3186. https://doi.org/10.1039/c9cs00806c

Monteiro MC, Goyal A, Moerland P, Koper MT (2021) Understanding cation trends for hydrogen evolution on platinum and gold electrodes in alkaline media. ACS Catal 11(23):14328–14335. https://doi.org/10.1021/acscatal.1c04268

Nordin NAHM, Ismail AF, Yahya N (2017) Zeolitic imidazole framework 8 decorated graphene oxide (ZIF-8/GO) mixed matrix membrane (MMM) for CO_2/CH_4 separation. J Teknol. https://doi.org/10.11113/jt.v79.10438

Oh NK, Seo J, Lee S, Kim HJ, Kim U, Lee J, Han Y-K, Park H (2021) Highly efficient and robust noble-metal free bifunctional water electrolysis catalyst achieved via complementary charge transfer. Nat Commun 12(1):1–12. https://doi.org/10.1038/s41467-021-24829-8

Pan Y, Liu Y, Zeng G, Zhao L, Lai Z (2011) Rapid synthesis of zeolitic imidazolate framework-8 (ZIF-8) nanocrystals in an aqueous system. Chem Commun 47(7):2071–2073. https://doi.org/10.1039/c0cc05002d

Perera F (2018) Pollution from fossil-fuel combustion is the leading environmental threat to global pediatric health and equity: solutions exist. Int J Environ Res Public Health 15(1):16. https://doi.org/10.3390/ijerph15010016

Pu Z, Cheng R, Zhao J, Hu Z, Li C, Li W, Wang P, Amiinu IS, Wang Z, Wang M, Chen D (2020) Anion-modulated platinum for high-performance multifunctional electrocatalysis toward HER, HOR, and ORR. Iscience 23(12):101793. https://doi.org/10.1016/j.isci.2020.101793

Qiao B, Wang A, Yang X, Allard LF, Jiang Z, Cui Y, Liu J, Li J, Zhang T (2011) Single-atom catalysis of CO oxidation using Pt_1/FeO_x. Nat Chem 3(8):634–641. https://doi.org/10.1038/nchem.1095

Rahmawati A, Shih CF, Imae T (2020) Film sensor of a ligand-functionalized cellulose nanofiber for the selective detection of copper and cesium ions. Polym J 52(10):1235–1243. https://doi.org/10.1038/s41428-020-0377-y

Sarfraz A, Raza AH, Mirzaeian M, Abbas Q, Raza R (2020) Electrode materials for fuel cells. In Reference module in materials science and materials engineering. Elsevier BV. https://doi.org/10.1016/B978-0-12-803581-8.11742-4

Shah KJ, Imae T (2016) Selective gas capture ability of gas-adsorbent-incorporated cellulose nanofiber films. Biomacromolecules 17(5):1653–1661. https://doi.org/10.1021/acs.biomac.6b00065

Shah KJ, Imae T (2017) Photoinduced enzymatic conversion of CO_2 gas to solar fuel on functional cellulose nanofiber films. J Mater Chem A 5(20):9691–9701. https://doi.org/10.1039/c7ta01861d

Sun X, Xu K, Fleischer C, Liu X, Grandcolas M, Strandbakke R, Bjørheim T, Norby T, Chatzitakis A (2018) Earth-abundant electrocatalysts in proton exchange membrane electrolyzers. Catalysts 8(12):657. https://doi.org/10.3390/catal8120657

Taherian R, Ghorbani MM, Nasr M, Kiahosseini SR (2018) Fabrication and investigation of polymer-based carbon composite as gas diffusion layer of proton exchange membrane of fuel cells. Mater Sci 1(1):1. https://doi.org/10.18063/msacm.v2i1.611

Tangkitthanachoke P, Petcharoen K, Paradee N, Sangwan W, Sirivat A (2017) Flexible and stretchable electrode based on multiwalled carbon nanotube/deproteinized natural rubber composites. Polym Eng Sci 57(12):1356–1366. https://doi.org/10.1002/pen.2451

Wang C, DeKrafft KE, Lin W (2012) Pt nanoparticles@ photoactive metal–organic frameworks: efficient hydrogen evolution via synergistic photoexcitation and electron injection. J Am Chem Soc 134(17):7211–7214. https://doi.org/10.1021/ja300539p

Wang P, Zhao J, Li X, Yang Y, Yang Q, Li C (2013) Assembly of ZIF nanostructures around free Pt nanoparticles: efficient size-selective catalysts for hydrogenation of alkenes under mild conditions. Chem Commun 49(32):3330–3332. https://doi.org/10.1039/c3cc39275a

Wei J, Ning F, Bai C, Zhang T, Lu G, Wang H, Li Y, Shen Y, Fu X, Li Q, Jin H, Zhou X (2020) An ultra-thin, flexible, low-cost and scalable gas diffusion layer composed of carbon nanotubes for high-performance fuel cells. J Mater Chem A 8(12):5986–5994. https://doi.org/10.1039/c9ta13944c

Wu YN, Zhou M, Zhang B, Wu B, Li J, Qiao J, Guan X, Li F (2014) Amino acid assisted templating synthesis of hierarchical zeolitic imidazolate framework-8 for efficient arsenate removal. Nanoscale 6(2):1105–1112. https://doi.org/10.1039/c3nr04390h

Xu SJ, Shen Q, Chen GE, Xu ZL (2018) Novel β-CD@ ZIF-8 nanoparticles-doped poly (m-phenylene isophthalamide) (PMIA) thin-film nanocomposite (TFN) membrane for organic solvent nanofiltration (OSN). ACS Omega 3(9):11770–11787. https://doi.org/10.1021/acsomega.8b01808

Zhang H, An P, Zhou W, Guan BY, Zhang P, Dong J, Lou XW (2018a) Dynamic traction of lattice-confined platinum atoms into mesoporous carbon matrix for hydrogen evolution reaction. Sci Adv 4(1):6657. https://doi.org/10.1016/j.jelechem.2021.115076

Zhang Y, Jia Y, Li M, Hou LA (2018b) Influence of the 2-methylimidazole/zinc nitrate hexahydrate molar ratio on the synthesis of zeolitic imidazolate framework-8 crystals at room temperature. Sci Rep 8(1):1–7. https://doi.org/10.1038/s41598-018-28015-7

Zhang C, Wang P, Li W, Zhang Z, Zhu J, Pu Z, Zhao Y, Mu S (2020) MOF-assisted synthesis of octahedral carbon-supported PtCu nanoalloy catalysts for an efficient hydrogen evolution reaction. J Mater Chem A 8(37):19348–19356